PHYSICAL REVIEW RESEARCH **6**, L022048 (2024)

Letter

180 °-twisted bilayer $ReSe_2$ as an artificial noncentrosymmetric semiconductor

S. Akatsuka,[1] M. Sakano,[1] T. Yamamoto,[1] T. Nomoto,[2] R. Arita,[2,3] R. Murata,[4] T. Sasagawa,[4] K. Watanabe,[5] T. Taniguchi,[6] N. Mitsuishi,[3] M. Kitamura,[7,8] K. Horiba,[8] K. Sugawara,[9,10] S. Souma,[9] T. Sato,[9] H. Kumigashira,[11] K. Shinokita,[12] H. Wang,[12] K. Matsuda,[12] S. Masubuchi,[13] T. Machida,[13] and K. Ishizaka[1,3]

[1]*Quantum-Phase Electronics Center and Department of Applied Physics, The University of Tokyo, Bunkyo-ku, Tokyo 113-8656, Japan*
[2]*Research Center for Advanced Science and Technology, The University of Tokyo, Meguro-ku, Tokyo 153-8904, Japan*
[3]*RIKEN Center for Emergent Matter Science (CEMS), Wako, Saitama 351-0198, Japan*
[4]*Materials and Structures Laboratory, Tokyo Institute of Technology, Yokohama, Kanagawa 226-8503, Japan*
[5]*Research Center for Electronic and Optical Materials, National Institute for Materials Science, 1-1 Namiki, Tsukuba 305-0044, Japan*
[6]*Research Center for Materials Nanoarchitectonics, National Institute for Materials Science, 1-1 Namiki, Tsukuba 305-0044, Japan*
[7]*Photon Factory, Institute of Materials Structure Science, High energy Accelerator Research Organization (KEK), Tsukuba 305-0801, Japan*
[8]*Institute for Advanced Synchrotron Light Source, National Institute for Quantum Science and Technology (QST), Sendai 980-8579, Japan*
[9]*Department of Physics, Graduate School of Science, and Advanced Institute for Materials Research (WPI-AIMR), Tohoku University, Sendai 980-8578, Japan*
[10]*Precursory Research for Embryonic Science and Technology (PRESTO), Japan Science and Technology Agency (JST), Tokyo 102-0076, Japan*
[11]*Institute of Multidisciplinary Research for Advanced Materials (IMRAM), Tohoku University, Sendai 980-8577, Japan*
[12]*Institute of Advanced Energy, Kyoto University, Uji, Kyoto 611-0011, Japan*
[13]*Institute of Industrial Science, The University of Tokyo, Meguro-ku, Tokyo 153-8505, Japan*

(Received 24 September 2023; revised 4 February 2024; accepted 25 April 2024; published 3 June 2024)

We have fabricated a 180 °-twisted bilayer $ReSe_2$ by stacking two centrosymmetric monolayer $ReSe_2$ flakes in opposite directions, which is expected to cause the loss of spatial inversion symmetry. We successfully observed spatial inversion-symmetry breaking, in contrast to the monolayer and natural bilayer $ReSe_2$ by the second harmonic generation. ARPES measurements further revealed emergent band dispersions in the 180 °-twisted bilayer $ReSe_2$, distinct from those of the monolayer $ReSe_2$ used in its fabrication. The band calculation shows the finite lifting of spin degeneracy ($\sim$50 meV) distinct from natural monolayer and bilayer $ReSe_2$, which demonstrates that the spin-momentum locked state leading to Berry curvature related phenomena can be realized even with the stacking of centrosymmetric monolayers.

DOI: 10.1103/PhysRevResearch.6.L022048

Advances in the fabrication techniques for exfoliated two-dimensional flakes and their van der Waals heterostructures have provided a platform for manipulating material symmetries through stacking order [1–4]. Among the various symmetries, spatial inversion symmetry is important in determining electronic structure and physical properties. One of the most representative examples is group VI transition metal dichalcogenide (TMD) semiconductors such as MoS_2. Monolayer MoS_2 has a noncentrosymmetric crystal structure with threefold rotational symmetry, which lifts the spin degeneracy at the Brillouin zone corners by spin-orbit interactions [5–8], leading to Berry curvature related phenomena appearing in nonlinear transport properties and optoelectronic properties [5–12]. The bilayer system has two distinct stacking orders: $2H$ and $3R$ type, in which the adjacent layers are stacked with 180 ° and 0 ° twisting [13]. The former recovers the spatial inversion symmetry, and the net spin polarization cancels out [13,14]. The latter maintains the breaking of spatial inversion symmetry [13] and, recently, emergent ferroelectricities in 0 °-stacked bilayer systems have been reported [3,4].

On the other hand, there are examples where the stacking order, regardless of the stacking of centrosymmetric monolayers, breaks the spatial inversion symmetry in a bilayer system. T_d-WTe_2 [15–22] is a well-known striking material. The crystal structure of the monolayer WTe_2 is centrosymmetric and is classified as a distorted $1T$ type (CdI_2 type) in the TMD family, which is defined by a network of edge-sharing WTe_6 octahedra [Fig. 1(a)]. The distinctive feature of the crystal symmetry of bulk T_d-WTe_2 is that adjacent layers stack in opposite directions in nature, in contrast to the usual $1T$ -type bulk TMD families (e.g., $HfSe_2$ [23–25], $TiSe_2$ [23,24,26], and $ReSe_2$ [27]) which have spatial inversion symmetry independent of the number of layers. This 180 °-twisted stacking breaks the spatial inversion symmetry in bilayer WTe_2, where the spin splitting of approximately 0.1 eV has been observed by microfocused angle-resolved photoemission spectroscopy (μ-ARPES) [19,22]. Inspired by these previous studies, we can expect that, in principle, the magnitude of spin splitting

---

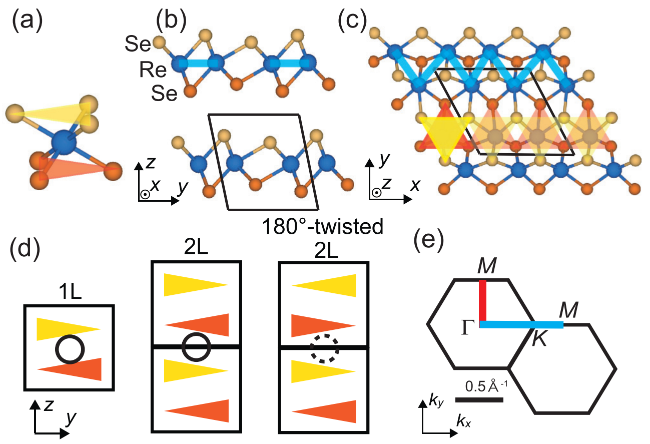

FIG. 1. (a) The typical nondistorted octahedral coordination for the T-type TMD. The yellow (orange) triangle indicates the orientation of the top (bottom) Se triangular networks. (b), (c) Side view (b) and top view (c) of the distorted T-type crystal structure of $ReSe_2$. The black frames in (c) indicate a unit cell for the monolayer (1L) $ReSe_2$. The light blue segments represent the Re zigzag-chain-like structure. (d) Schematic views of the crystal symmetries for 1L, bilayer (2L), and 180 °-twisted 2L $ReSe_2$. The black rectangle represents each unit of the $ReSe_2$ layer. The black circles represent the inversion centers. The dotted circle depicted for the antiparallel 2L $ReSe_2$ represents a lack of the inversion center by their stacking order. (e) Two-dimensional Brillouin zone for the 1L, 2L, and 180 °-twisted 2L $ReSe_2$. The Brillouin zone is slightly shear deformed from a regular hexagon. However, in this study, we represent Γ-K (Γ-M) as the direction parallel (perpendicular) to the Re zigzag chain because the actual high-symmetrical K point (M point) locates only 0.008 (0.013) $Å^{-1}$ off the k_x (k_y) axis.

could be controlled by artificially changing the stacking angle, even when stacking with centrosymmetric $1T$ -type TMD monolayers.

In this study, we focus on the layered semiconductor $ReSe_2$. Reflecting the strong spin-orbit interaction of the Re 5d orbitals, the effect of inversion-symmetry breaking is expected to appear in the nonlinear optical properties and electronic band dispersions. The direct and indirect band gaps of bulk $ReSe_2$ are 1.40 eV [28] and 1.18–1.19 eV [29,30], respectively. $ReSe_2$ is known to have a weak interlayer coupling, making it possible to fabricate down to a monolayer by mechanical exfoliation [31–34] with an exitonic direct band gap of 1.50 eV [32]. The overall electronic structure does not change significantly regardless of the number of layers, indicating weak van der Waals interactions between the layers [32,34,35]. $ReSe_2$ has a distorted $1T$ -type triclinic crystal structure (space group $P\bar{1}$), as shown in Figs. 1(a)–1(c). The opposing Se-triangle networks (shown in yellow and orange) sandwich the distorted Re layer characterized by Re zigzag chains (indicated by the light blue lines). As shown in Fig. 1(d), we schematically illustrate the concept of this study for the artificial fabrication of noncentrosymmetric bilayer $ReSe_2$. The essence extracted from the crystal structure of monolayer (1L) $ReSe_2$ is represented by two opposing Se-triangular networks (yellow and orange triangles) and the inversion center (black circle). In the natural bilayer case, an inversion center appeared between the layers. However, in the 180 °-twisted 2L $ReSe_2$, the triangles face the same direction across the interlayer, such that the inversion center does not appear anywhere between the layers, shown as a dotted circle. Although there are translational degrees of freedom upon stacking in the x and y directions, the fabricated structure cannot have an inversion center in any cases. In 180 °-twisted 2L $ReSe_2$, spin degeneracy is expected to be lifted in reciprocal space owing to spin-orbit interaction, which has the potential to give rise to physical properties related to the Berry curvature, such as the shift current [11], nonlinear Hall effect [12], and ferroelectric switching [18].

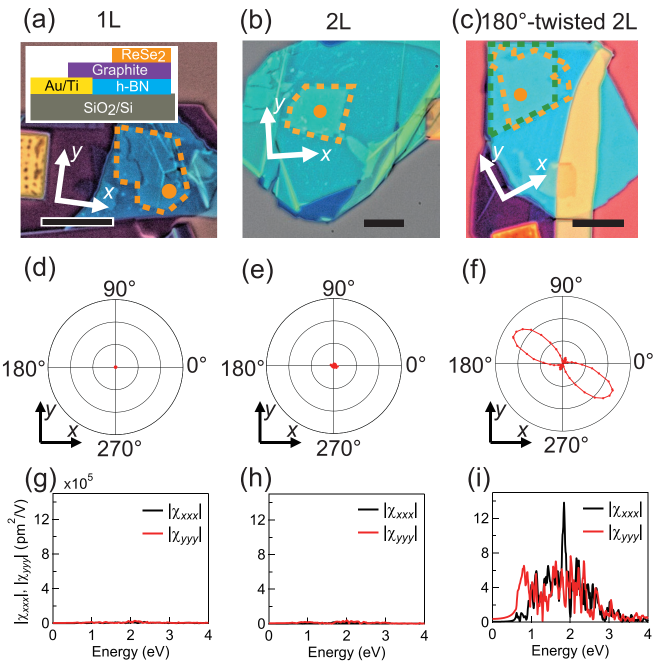

FIG. 2. (a)–(c) Optical microscope images of the samples for ARPES and SHG measurement. The inset in (a) shows a schematic of the sample. The black segments represent 10 μm. The monolayer $ReSe_2$ flakes used are outlined with orange and green broken lines. Orange circles indicate the SHG measurement position. (d)–(f) Polar plot of the SH intensity from 1L, 2L, and 180 °-twisted $ReSe_2$. Linear-polarized component of the SHG parallel to the linear polarization of the incident light is detected. For (f), the data between 0 ° and 180 ° are symmetrized and displayed in the region between 180 ° and 360 °. (g)–(i) The calculated second order electrical susceptibility χ_{xxx} and χ_{yyy} for 1L, 2L, and 180 °-twisted $ReSe_2$.

The 180 °-twisted 2L $ReSe_2$ sample was fabricated using an all-dry pick-up [36,37], tear and stack [38], and flip method [39] using an Elvacite 2552C copolymer inside a glove box chamber [40]. In addition, we also prepared the monolayer and natural bilayer $ReSe_2$ samples for control experiments. During fabrication, hexagonal boron nitride (hBN), graphite, and $ReSe_2$ flakes were sequentially picked using a polymer stamp. The assembled heterostructure was transferred to another polymer stamp at room temperature to turn it over. Then it was dropped onto a SiO_2/Si substrate with a prepatterned metal electrode, as schematically shown in the inset of Fig. 2(a). Optical microscope images for 1L, 2L, and 180 °-twisted 2L $ReSe_2$ are shown in Figs. 2(a)–2(c), respectively. The $ReSe_2$ flakes were approximately 10 μm in size, outlined with orange and green broken lines. In this study, we performed optical second harmonic generation (SHG) measurements at room temperature [40] to examine the breaking of the spatial inversion symmetry. In addition, to observe the emergent electronic band dispersions in 180 °-twisted 2L ReSe$_2$ we performed μ-ARPES measurements using a photon energy of 100 eV and a spot size of $12 \times 15\ \mu\text{m}^2$ at BL28 in the Photon Factory, KEK [41]. The total energy resolution was set at 35 meV. During the measurement, a sample manipulator temperature was kept below 20 K. The Fermi levels (E_F) were determined using polycrystalline gold electrically connected to the respective samples. The band structure calculations [40] were performed using the Vienna *Ab initio* Simulation Package (VASP) [42,43]. The crystal structures were determined by structure optimization taking into account the van der Waals correction with the density functional theory (DFT)-D3 method [44]. The second-order susceptibility calculations were performed based on the tight-binding model constructed from the DFT electronic structures through the WANNIER90 code [45].

Figures 2(d)–2(f) show the polar-angle dependences of the normalized SHG signals from the 1L, 2L, and 180 °-twisted 2L ReSe$_2$ samples. The orange circles indicate the measurement areas on the topmost ReSe$_2$ flakes (depicted with the orange frames). The SHG signals are detected only from 180 °-twisted 2L; however, they are negligible from 1L and 2L reflecting the spatial inversion symmetry of natural ReSe$_2$ crystal independent of the number of layers. (See Supplemental Material [40] for the detailed SHG simulations and measurements.) These experimental results are consistent with the description using simple structure models shown in Fig. 1(d). To compare with the experimental observation, we calculated second-order susceptibility χ_{xxx} and χ_{yyy}, which represent the SHG response parallel to the incident light polarization [along x and y, respectively, as shown in Fig. 1(c)] [40]. The energy dependences of χ_{xxx} and χ_{yyy} for 1L, 2L, and 180 °-twisted 2L are shown in Fig. 2(g). In contrast to the negligible χ_{xxx} and χ_{yyy} for 1L and 2L, the finite χ_{xxx} and χ_{yyy} were demonstrated for 180 °-twisted 2L, indicating that the observed SHG signal was consistent with the design of the breaking of spatial inversion symmetry. The crystal structure of 180 °-twisted 2L used for the calculations and the simulated polar pattern of the SH intensity are shown in the Supplemental Material [40].

We performed ARPES measurements on 1L, 2L, and 180 °-twisted 2L ReSe$_2$ to observe their two-dimensional electronic structures. Figures 3(a)–3(c) show the ARPES intensity mapping at the constant energies of $E - E_\text{F} = -1.3\,\text{eV}$. The constant energy contours for the highest valence band (HVB) observed in Figs. 3(a)–3(c) clearly show anisotropic contours of the isoenergetic surface that are not closed along the k_y direction, reflecting the quasi-one-dimensional Re zigzag chain along x as shown in Fig. 1(c). Figures 3(d)–3(f) show the ARPES images along the k_y (Γ-M, left side) and k_x (Γ-K-M, right side) directions [Fig. 1(e)] for 1L, 2L, and 180 °-twisted 2L ReSe$_2$, respectively. Considering that the band dispersions at $\pm k_x$ ($\pm k_y$) are linked via time-reversal symmetry and should be the same when ignoring the spin degrees of freedom, the ARPES intensities in Figs. 3(d)–3(f) display the sums of them for better visibility. In the energy region from the Fermi energy to $E = E_\text{F} - 0.8\,\text{eV}$, which is omitted in Fig. 3, no bands originating from ReSe$_2$ are observed, whereas there are certain signals from graphite. This is consistent with previous studies of 1L and 2L ReSe$_2$ [33,34]. For better visualization of the band dispersions, curvature plots [46] for the respective ARPES images are shown in Figs. 3(g)–3(i). Comparing 1L, 2L, and 180 °-twisted 2L, a clear difference became apparent when focusing on the HVB. A recent precise ARPES study revealed that the valence band maximum (VBM) of bulk ReSe$_2$ is located off the high symmetry point along the k_y direction ($k_y \sim 0.15\,\text{Å}^{-1}$) at $k_z = \pi/c$ with upward convex-shaped dispersions [47,48]. As discussed below, the ARPES

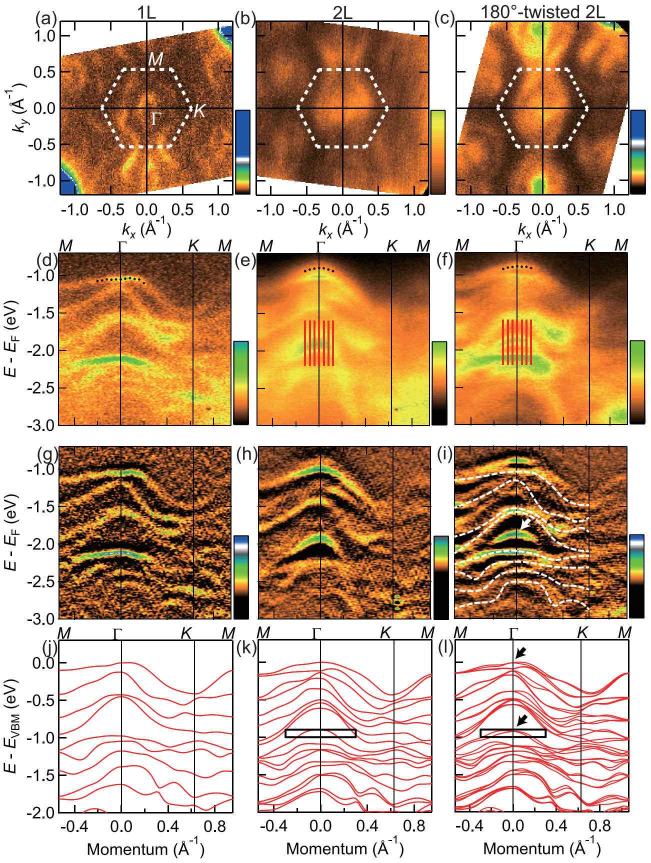

FIG. 3. (a)–(c) ARPES mapping images at a constant energy of $E - E_\text{F} = -1.3\,\text{eV}$ of 1L, 2L, and 180 °-twisted 2L ReSe$_2$. White broken lines represent the Brillouin zones for 1L, 2L, and 180 °-twisted 2L. (d)–(f) Combined ARPES images along the Γ-M (k_y) and Γ-K-M (k_x) directions. Those ARPES images along the k_x (k_y) direction are symmetrized with respect to k_x (k_y) = 0. Black circle markers represent the peak positions of the ARPES spectra for the respective highest valence bands. Red segments in (e), (f) represent energy cuts for the energy distribution curves shown in Figs. 4(c) and 4(d), respectively. (g)–(i) Images obtained by the curvature analysis [46] for the ARPES images in (d)–(f). White broken lines in (g) represent the band dispersions of monolayer ReSe$_2$ obtained from the ARPES image, which are inevitably observed from the 180 °-twisted 2L ReSe$_2$ samples. (j)–(l) Calculated band dispersions of 1L, 2L, and 180 °-twisted 2L ReSe$_2$. The origins of energy axes are set as the maximum of the valence band (VBM). The black rectangles in (k), (l) indicate the area of the magnified view in Figs. 4(a) and 4(b), respectively.

results demonstrate that the two-dimensional confinement of the electronic structure causes a shift in the position of the VBM. The detailed analysis of our result on 1L $\mathrm{ReSe_2}$ shows that the HVB is almost flat with 40 meV dispersion within the $k = \pm 0.15$ Å^{-1} range around the Γ point, as indicated by the markers in Fig. 3(d) that represent the positions of the intensity peaks. In contrast to 1L $\mathrm{ReSe_2}$, 2L and 180°-twisted 2L $\mathrm{ReSe_2}$ exhibited upward convex-shaped HVBs with the VBM at the Γ point as shown in Figs. 3(e) and 3(f). Figures 3(j)–3(l) show the band dispersions obtained from first-principles band calculations with optimizing the crystal structure [40] for 1L, 2L, and 180°-twisted 2L $\mathrm{ReSe_2}$, respectively. Compared to the calculation results using the fixed atomic coordinates of bulk crystal [27,40], the calculation with structural optimization tends to form flatter HVBs around the Γ point, which reproduces the observed band dispersions for 1L and 2L $\mathrm{ReSe_2}$. Although the precise crystal structure of the 180°-twisted 2L $\mathrm{ReSe_2}$ remains undetermined, the calculation result assuming one of the possible crystal structures [40] appears plausible, as it also reproduces the ARPES results well.

Subsequently, we discuss the effect of 180°-twisted stacking on band dispersions in $\mathrm{ReSe_2}$. In Figs. 3(j)–3(l), we can observe that the number of bands in the band calculations doubles from 1L to 2L, and from 2L to 180°-twisted 2L $\mathrm{ReSe_2}$, respectively. The former was owing to the bilayer splitting caused by doubling the number of atoms in a unit cell. However, the latter doubling was due to the breaking of spatial inversion symmetry at 180°-twisted 2L induced by staggered stacking [Fig. 1(d)], leading to the lifting of spin degeneracy. The maximum spin-splitting energy was estimated to be approximately 70 meV in this calculation. To evaluate the possible spin-split band dispersions appearing in the experimental results, we reviewed the ARPES images of the 180°-twisted 2L $\mathrm{ReSe_2}$ in Figs. 3(f) and 3(i). Note that the ARPES intensities from the nonoverlapped and/or nonhybridized 1L $\mathrm{ReSe_2}$ flakes were inevitable because the beam-spot size was comparable to the sample size. In Fig. 3(f), we show a guide for the eyes depicted with broken white curves representing the band dispersions of 1L $\mathrm{ReSe_2}$ extracted from the ARPES image in Fig. 3(d). In addition to the HVB, a band dispersion appearing in 180°-twisted 2L $\mathrm{ReSe_2}$ as indicated by a white arrow in Fig. 3(i) is observed around $E - E_\mathrm{F} = -1.9$ eV at the Γ point where the band dispersion does not exist in the 1L $\mathrm{ReSe_2}$ [Fig. 3(f)]. In a comparison of the calculated band dispersions between 2L and 180°-twisted 2L $\mathrm{ReSe_2}$ in Figs. 3(k) and 3(l), the corresponding band dispersions are well isolated from the other band dispersions. As expected from the symmetry requirement shown in Fig. 1(d), only 180°-twisted 2L $\mathrm{ReSe_2}$ [Fig. 3(l)] exhibited spin-split band dispersion.

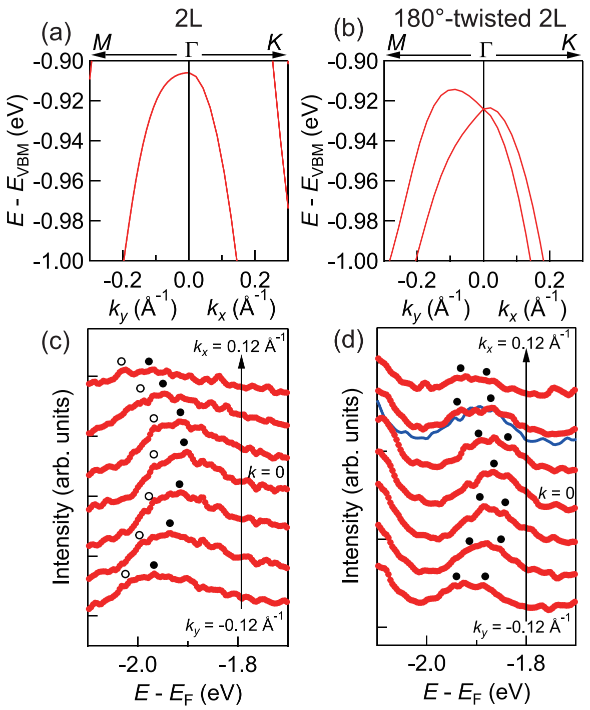

FIG. 4. (a), (b) Enlarged views of the calculational band dispersion in 2L and 180°-twisted 2L $\mathrm{ReSe_2}$. The corresponding regions are indicated by the black rectangle in Figs. 3(k) and 3(l). (c), (d) EDCs extracted from the ARPES images of 2L and 180°-twisted 2L $\mathrm{ReSe_2}$ as denoted by the red segments in Figs. 3(e) and 3(f), respectively. Black solid circle markers represent the peak positions. Open circle markers in (c) represent peak positions from the area with different possible chemical potentials. The blue curve shows the EDC at $k = 0$ is replaced to indicate the broadening of the spectrum of $k_x = 0.12$ as a representative. The thinner blue curve represents the EDC at $k = 0$, shifted by 27 meV and reused to suggest the broadening of the spectrum at $k_x = 0.08$ Å^{-1} as a representative example.

Finally, we focus on the experimental results of the band dispersion at 180°-twisted 2L $\mathrm{ReSe_2}$ to examine whether there is a footprint of spin-split band dispersion. Magnified views of the calculated band dispersions of 2L and 180°-twisted 2L $\mathrm{ReSe_2}$, corresponding to the area indicated by the black rectangles in Figs. 3(k) and 3(l), are shown in Figs. 4(a) and 4(b), respectively. Here, we can see band splitting with lifting of the spin degeneracy only for 180°-twisted 2L $\mathrm{ReSe_2}$. Spin splitting is larger in the k_y direction, with a maximum of approximately 50 meV. We performed calculations for three different x, y shifts on stacking and identified that the energies of spin splitting were almost similar [40]. The energy distribution curves (EDCs) extracted from the ARPES images at 2L and 180°-twisted 2L $\mathrm{ReSe_2}$ in Figs. 3(e) and 3(f) are shown in Figs. 4(c) and 4(d), respectively. The corresponding energy cuts from $k = -0.12$ to 0.12 Å^{-1} are indicated by the red lines in Figs. 3(e) and 3(f). Regarding the EDCs of 180°-twisted 2L $\mathrm{ReSe_2}$, when comparing the EDC spectra at the Γ point and away from the Γ point, it appears that the latter exhibited a somewhat broader shape. (For comparison, the EDC at $k_x = 0.08$ Å^{-1} is overlaid on the EDC at $k_x = 0$, depicted in blue, as a representative example.) In contrast, the EDCs of 2L $\mathrm{ReSe_2}$ also exhibited broad two-peak-like structures but rather with parallel dispersions, as indicated by the black solid and open circle markers. The weak peaks indicated by open circles do not appear in the calculation and their origin is not clear, but considering a rather broad and hazy ARPES image obtained from 2L $\mathrm{ReSe_2}$, they may be attributed to ARPES intensities originating from inhomogeneous areas, e.g., with different chemical potentials. To conclusively determine the presence or absence of the approximately 50 meV band splitting, as expected by combining SHG experiments and first-principles band calculations, future challenges for this study include direct observations utilizing a nanofocused ARPES experiment with a smaller spot size and/or a microfocused spin-resolved ARPES experiment.

In summary, we fabricated a 180 °-twisted 2L $\mathrm{ReSe_2}$ with the breaking of spatial inversion symmetry, whereas 1L and natural 2L $\mathrm{ReSe_2}$ possessed symmetry. We have detected the SHG signal only in the 180 °-twisted 2L $\mathrm{ReSe_2}$, in good agreement with the calculation, indicating the breaking of the spatial inversion symmetry. Our ARPES study also indicated the stacking-dependent emergent electronic band dispersions in these $\mathrm{ReSe_2}$ thin flakes. This study successfully paves the way for the artificial creation of noncentrosymmetric two-dimensional systems by stacking inversion-symmetric two-dimensional crystals.

This research was partly supported by a CREST project (Grants No. JPMJCR18T1 and No. JPMJCR20B4) from the Japan Science and Technology Agency (JST), Japan Society for the Promotion of Science KAKENHI (Grants-in-Aid for Scientific Research) (Grants No. JP20H01834, No. JP20H05664, No. JP21H01012, No. JP21H01757, No. JP21H04652, No. JP21H05232, No. JP21H05233, No. JP21H05234, No. JP21H05235, No. JP21H05236, No. JP21K18181, No. JP22K18986, No. JP23H02052, and No. JP23H05469), JST SPRING (Grant No. JPMJSP2106), and JST PRESTO (Grant No. JPMJPR20A8). K.W. and T.T. acknowledge support from World Premier International Research Center Initiative (WPI), MEXT, Japan. This work was partly performed under the approval of the Photon Factory Program Advisory Committee (Proposal No. 2021G141, No. 2023G088, No. 2018S2-001, and No. 2021S2-001).

[1] A. K. Geim and I. V. Grigorieva, Van der Waals heterostructures, Nature (London) **499**, 419 (2013).

[2] T. Akamatsu, T. Ideue, L. Zhou, Y. Dong, S. Kitamura, M. Yoshii, D. Yang, M. Onga, Y. Nakagawa, K. Watanabe, T. Taniguchi, J. Laurienzo, J. Huang, Z. Ye, T. Morimoto, H. Yuan, and Y. Iwasa, A van der Waals interface that creates in-plane polarization and a spontaneous photovoltaic effect, Science **372**, 68 (2021).

[3] K. Yasuda, X. Wang, K. Watanabe, T. Taniguchi, and P. Jarillo-Herrero, Stacking-engineered ferroelectricity in bilayer boron nitride, Science **372**, 1458 (2021).

[4] X. Wang, K. Yasuda, Y. Zhang, S. Liu, K. Watanabe, T. Taniguchi, J. Hone, L. Fu, and P. Jarillo-Herrero, Interfacial ferroelectricity in rhombohedral-stacked bilayer transition metal dichalcogenides, Nat. Nanotechnol. **17**, 367 (2022).

[5] D. Xiao, G.-B. Liu, W. Feng, X. Xu, and W. Yao, Coupled spin and valley physics in monolayers of $\mathrm{MoS_2}$ and other group-VI dichalcogenides, Phys Rev. Lett. **108**, 196802 (2012).

[6] H. Zeng, J. Dai, W. Yao, D. Xiao, and X. Cui, Valley polarization in $\mathrm{MoS_2}$ monolayers by optical pumping, Nat. Nanotechnol. **7**, 490 (2012).

[7] K. F. Mak, K. He, J. Shan, and T. F. Heinz, Control of valley polarization in monolayer $\mathrm{MoS_2}$ by optical helicity, Nat. Nanotechnol. **7**, 494 (2012).

[8] T. Cao, G. Wang, W. Han, H. Ye, C. Zhu, J. Shi, Q. Niu, P. Tan, E. Wang, B. Liu, and J. Feng, Valley-selective circular dichroism of monolayer molybdenum disulphide, Nat. Commun. **3**, 887 (2012).

[9] G. Sundaram and Q. Niu, Wave-packet dynamics in slowly perturbed crystals: Gradient corrections and Berry-phase effects, Phys. Rev. B **59**, 14915 (1999).

[10] D. Xiao, M.-C. Chang, and Q. Niu, Berry phase effects on electronic properties, Rev. Mod. Phys. **82**, 1959 (2010).

[11] J. E. Moore and J. Orenstein, Confinement-induced Berry phase and helicity-dependent photocurrents, Phys. Rev. Lett. **105**, 026805 (2010).

[12] I. Sodemann and L. Fu, Quantum nonlinear Hall effect induced by Berry curvature dipole in time-reversal invariant materials, Phys. Rev. Lett. **115**, 216806 (2015).

[13] R. Suzuki, M. Sakano, Y. J. Zhang, R. Akashi, D. Morikawa, A. Harasawa, K. Yaji, K. Kuroda, K. Miyamoto, T. Okuda, K. Ishizaka, R. Arita, and Y. Iwasa, Valley-dependent spin polarization in bulk $\mathrm{MoS_2}$ with broken inversion symmetry, Nat. Nanotechnol. **9**, 611 (2014).

[14] Y. Li, Y. Rao, K. F. Mak, Y. You, S. Wang, C. R. Dean, and T. F. Heinz, Probing symmetry properties of few-layer $\mathrm{MoS_2}$ and h-BN by optical second-harmonic generation, Nano Lett. **13**, 3329 (2013).

[15] M. N. Ali, J. Xiong, S. Flynn, J. Tao, Q. D. Gibson, L. M. Schoop, T. Liang, N. Haldolaarachchige, M. Hirschberger, N. P. Ong, and R. J. Cava, Large, non-saturating magnetoresistance in $\mathrm{WTe_2}$, Nature (London) **514**, 205 (2014).

[16] A. A. Soluyanov, D. Gresch, Z. Wang, Q. Wu, M. Troyer, X. Dai, and B. A. Bernevig, Type-II Weyl semimetals, Nature (London) **527**, 495 (2015).

[17] Z. Fei, T. Palomaki, S. Wu, W. Zhao, X. Cai, B. Sun, P. Nguyen, J. Finney, X. Xu, and D. H. Cobden, Edge conduction in monolayer $\mathrm{WTe_2}$, Nat. Phys. **13**, 677 (2017).

[18] Z. Fei, W. Zhao, T. A. Palomaki, B. Sun, M. K. Miller, Z. Zhao, J. Yan, X. Xu, and D. H. Cobden, Ferroelectric switching of a two-dimensional metal, Nature (London) **560**, 336 (2018).

[19] I. Cucchi, I. Gutiérrez-Lezama, E. Cappelli, S. M. Walker, F. Y. Bruno, G. Tenasini, L. Wang, N. Ubrig, C. Barreteau, E. Giannini, M. Gibertini, A. Tamai, A. F. Morpurgo, and F. Baumberger, Microfocus laser–angle-resolved photoemission on encapsulated mono-, bi-, and few-layer $1T'$-$\mathrm{WTe_2}$, Nano Lett. **19**, 554 (2019).

[20] H. Wang and X. Qian, Ferroelectric nonlinear anomalous Hall effect in few-layer $\mathrm{WTe_2}$, npj Comput. Mater. **5**, 119 (2019).

[21] J. Xiao, Y. Wang, H. Wang, C. D. Pemmaraju, S. Wang, P. Muscher, E. J. Sie, C. M. Nyby, T. P. Devereaux, X. Qian, X. Zhang, and A. M. Lindenberg, Berry curvature memory through electrically driven stacking transitions, Nat. Phys. **16**, 1028 (2020).

[22] M. Sakano, Y. Tanaka, S. Masubuchi, S. Okazaki, T. Nomoto, A. Oshima, K. Watanabe, T. Taniguchi, R. Arita, T. Sasagawa, T. Machida, and K. Ishizaka, Odd-even layer-number effect of valence-band spin splitting in $\mathrm{WTe_2}$, Phys. Rev. Res. **4**, 023247 (2022).

[23] F. K. McTaggart and A. D. Wadsley, The sulphides, selenides, and tellurides of titanium, zirconium, hafnium, and thorium.

I. Preparation and characterization, Aust. J. Chem. **11**, 445 (1958).

[24] D. L. Greenaway and R. Nitsche, Preparation and optical properties of group IV-VI$_2$ chalcogenides having CdI$_2$ structure, J. Phys. Chem. Solids **26**, 1445 (1965).

[25] H. P. B. Rimmington and A. A. Balchin, Crystal data for layer compounds in the series HfS$_x$Se$_{2-x}$, J. Mater. Sci. **9**, 343 (1974).

[26] F. J. Di Salvo, D. E. Moncton, and J. V. Waszczak, Electronic properties and superlattice formation in the semimetal TiSe$_2$, Phys. Rev. B **14**, 4321 (1976).

[27] N. W. Alcock and A. Kjekshus, The crystal structure of ReSe$_2$, Acta Chem. Scand. **19**, 79 (1965).

[28] C. H. Ho, P. C. Liao, Y. S. Huang, and K. K. Tiong, Temperature dependence of energies and broadening parameters of the band-edge excitons of ReS$_2$ and ReSe$_2$, Phys. Rev. B **55**, 15608 (1997).

[29] J. V. Marzik, R. Kershaw, K. Dwight, and A. Wold, Photoelectronic properties of ReS$_2$ and ReSe$_2$ single crystals, J. Solid State Chem. **51**, 170 (1984).

[30] C. H. Ho, Y. S. Huang, J. L. Chen, T. E. Dann, and K. K. Tiong, Electronic structure of ReS$_2$ and ReSe$_2$ from first-principles calculations, photoelectron spectroscopy, and electrolyte electroreflectance, Phys. Rev. B **60**, 15766 (1999).

[31] D. Wolverson, S. Crampin, A. S. Kazemi, A. Ilie, and S. J. Bending, Raman spectra of monolayer, few-layer, and bulk ReSe$_2$: An anisotropic layered semiconductor, ACS Nano **8**, 11154 (2014).

[32] A. Arora, J. Noky, M. Drüppel, B. Jariwala, T. Deilmann, R. Schneider, R. Schmidt, O. Del Pozo-Zamudio, T. Stiehm, A. Bhattacharya, P. Krüger, S. Michaelis de Vasconcellos, M. Rohlfing, and R. Bratschitsch, Highly anisotropic in-plane excitons in atomically thin and bulklike $1T'$-ReSe$_2$, Nano Lett. **17**, 3202 (2017).

[33] B. K. Choi, S. Ulstrup, S. M. Gunasekera, J. Kim, S. Y. Lim, L. Moreschini, J. S. Oh, S.-H. Chun, C. Jozwiak, A. Bostwick, E. Rotenberg, H. Cheong, I.-W. Lyo, M. Mucha-Kruczynski, and Y. J. Chang, Visualizing orbital content of electronic bands in anisotropic 2D semiconducting ReSe$_2$, ACS Nano **14**, 7880 (2020).

[34] L. S. Hart, S. M. Gunasekera, M. Mucha-Kruczynski, J. L. Webb, J. Avila, M. C. Asensio, and D. Wolverson, Interplay of crystal thickness and in-plane anisotropy and evolution of quasi-one dimensional electronic character in ReSe$_2$, Phys. Rev. B **104**, 035421 (2021).

[35] J. P. Echeverry and I. C. Gerber, Theoretical investigations of the anisotropic optical properties of distorted $1T$-ReS$_2$ and ReSe$_2$ monolayers, bilayers, and in the bulk limit, Phys. Rev. B **97**, 075123 (2018).

[36] S. Masubuchi, M. Morimoto, S. Morikawa, M. Onodera, Y. Asakawa, K. Watanabe, T. Taniguchi, and T. Machida, Autonomous robotic searching and assembly of two-dimensional crystals to build van der Waals superlattices, Nat. Commun. **9**, 1413 (2018).

[37] S. Masubuchi, E. Watanabe, Y. Seo, S. Okazaki, T. Sasagawa, K. Watanabe, T. Taniguchi, and T. Machida, Deep-learning-based image segmentation integrated with optical microscopy for automatically searching for two-dimensional materials, npj 2D Mater. Appl. **4**, 3 (2020).

[38] K. Kim, M. Yankowitz, B. Fallahazad, S. Kang, H. C. P. Movva, S. Huang, S. Larentis, C. M. Corbet, T. Taniguchi, K. Watanabe, S. K. Banerjee, B. J. LeRoy, and E. Tutuc, van der Waals heterostructures with high accuracy rotational alignment, Nano Lett. **16**, 1989 (2016).

[39] S. Masubuchi, M. Sakano, Y. Tanaka, Y. Wakafuji, T. Yamamoto, S. Okazaki, K. Watanabe, T. Taniguchi, J. Li, H. Ejima, T. Sasagawa, T. Machida, and K. Ishizaka, Dry pick-and-flip assembly of van der Waals heterostructures for microfocus angle-resolved photoemission spectroscopy, Sci. Rep. **12**, 10936 (2022).

[40] See Supplemental Material at http://link.aps.org/supplemental/10.1103/PhysRevResearch.6.L022048 for details of the sample fabrication, experimental condition of the second harmonic generation, and band calculations.

[41] M. Kitamura, S. Souma, A. Honma, D. Wakabayashi, H. Tanaka, A. Toyoshima, K. Amemiya, T. Kawakami, K. Sugawara, K. Nakayama, K. Yoshimatsu, H. Kumigashira, T. Sato, and K. Horiba, Development of a versatile micro-focused angle-resolved photoemission spectroscopy system with Kirkpatrick-Baez mirror optics, Rev. Sci. Instrum. **93**, 033906 (2022).

[42] G. Kresse and J. Furthmuller, Efficient iterative schemes for *ab initio* total-energy calculations using a plane-wave basis set, Phys. Rev. B **54**, 11169 (1996).

[43] G. Kresse and J. Furthmuller, Efficiency of *ab-initio* total energy calculations for metals and semiconductors using a plane-wave basis set, Comput. Mater. Sci. **6**, 15 (1996).

[44] S. Grimme, J. Antony, S. Ehrlich, and H. Krieg, A consistent and accurate *ab initio* parametrization of density functional dispersion correction (DFT-D) for the 94 elements H-Pu, J. Chem. Phys. **132**, 154104 (2010).

[45] A. A. Mostofi, J. R. Yates, Y.-S. Lee, I. Souza, D. Vanderbilt, and N. Marzari, WANNIER90: A tool for obtaining maximally-localised Wannier functions, Comput. Phys. Commun. **178**, 685 (2008).

[46] P. Zhang, P. Richard, T. Qian, Y.-M. Xu, X. Dai, and H. Ding, A precise method for visualizing dispersive features in image plots, Rev. Sci. Instrum. **82**, 043712 (2011).

[47] L. S. Hart, J. L. Webb, S. Dale, S. J. Bending, M. Mucha-Kruczynski, D. Wolverson, C. Chen, J. Avila, and M. C. Asensio, Electronic bandstructure and van der Waals coupling of ReSe$_2$ revealed by high-resolution angle-resolved photoemission spectroscopy, Sci. Rep. **7**, 5145 (2017).

[48] P. Eickholt, J. Noky, E. F. Schwier, K. Shimada, K. Miyamoto, T. Okuda, C. Datzer, M. Drüppel, P. Krüger, M. Rohlfing, and M. Donath, Location of the valence band maximum in the band structure of anisotropic $1T'$-ReSe$_2$, Phys. Rev. B **97**, 165130 (2018).